ADVANCED FUNCTIONAL MATERIALS
www.afm-journal.de

Stair-Stepping Mechanical Metamaterials with Programmable Load Plateaus

Chengjun Zeng, Liwu Liu, Yunqiang Hu, Wei Zhao, Xiaozhou Xin, Yanju Liu, and Jinsong Leng**

Materials with target load plateaus offer the potential for developing innovative vibration suppression and isolation systems for applications such as satellite platforms, submarines, and electric vehicles. However, implementing these materials can pose significant challenges. In this study, stair-stepping mechanical metamaterials with programmable load plateaus are presented, which are created via a three-level (unit, module, and 3D object) construction strategy. The strategy inspired by the inverse design concept achieves tunability in the number and properties of load plateaus within the force–displacement profiles of the metamaterials. This approach even yields appealing stair-stepping response patterns, as validated by experiments and finite element simulations. Promisingly, programming the unit from its initial configuration to a "zero stiffness" configuration enables these metamaterials excellent vibration isolation performance. Furthermore, two reversible methods are proposed for switching among various unit configurations, namely shape memory programming and supporting payload. This innovative design strategy for programmable load plateaus opens up new possibilities for creating metamaterials with customized force–displacement responses. It also provides opportunities to incorporate multimodal vibration isolation capabilities into precision devices.

1. Introduction

Metamaterials are intelligently designed materials that exhibit remarkable physical properties not naturally found in conventional materials. These properties are achieved through deliberate configuration design and precise spatial arrangement of periodic building blocks (often referred to as "meta-atoms").[1–3] Within the realm of metamaterials, mechanical metamaterials represent a burgeoning field. They harness various mechanisms like rotation,[4–6] buckling,[7,8] or folding[9,10] of these building blocks to achieve unconventional and counterintuitive properties and functionalities, including programmability,[11–13] self-determination,[14,15] and logical operations.[16,17] The counterintuitive mechanical properties exhibited by mechanical metamaterials primarily stem from the ability to manipulate their equivalent stiffness,[18] Poisson's ratio,[19] coefficient of thermal expansion,[20] and mass density. These mechanical metamaterials often possess one or more extraordinary mechanical parameters, such as negative or zero stiffness,[21,22] negative or zero Poisson's ratio,[23] and negative or zero coefficient of thermal expansion.[24]

Conventional vibration control techniques like vibration damping and vibration isolation have found extensive application in engineering. However, they encounter limitations when it comes to controlling and dissipating low-frequency and broadband vibration energy due to the constraints imposed by space and mass considerations.[25,26] The incorporation of mechanical metamaterials into structural or device design offers a promising solution by significantly enhancing the interaction between structures and low-frequency wave propagation, improving the control and dissipation of fluctuating energy.[27–29] The mechanical metamaterials are constructed by integrating building blocks with unique characteristics such as local resonance,[30] negative Poisson's ratio,[31,32] or quasi-zero stiffness (QZS).[33] These building blocks are attached or embedded strategically to achieve efficient attenuation or localized suppression of vibrations in the target frequency band. The so-called QZS metamaterials refer to materials with almost zero overall dynamic stiffness, while still maintaining robust load-bearing capabilities, essentially exhibiting high-static-low-dynamic properties.[34] Mechanically, these materials exhibit a plateau on the force–displacement curve, indicating that the payload remains nearly constant over a small displacement range, signifying zero tangential stiffness.[35] The classical QZS metamaterials are created by connecting positive and negative stiffness elements in parallel, where the negative stiffness elements can take the form of inclined springs, buckling beams, or magnetic rings.[36,37]

C. Zeng, L. Liu, Y. Hu, W. Zhao, X. Xin, Y. Liu
Department of Astronautical Science and Mechanics
Harbin Institute of Technology (HIT)
Harbin 150001, P. R. China
E-mail: yj_liu@hit.edu.cn

J. Leng
Center for Composite Materials and Structures
Harbin Institute of Technology (HIT)
Harbin 150080, P. R. China
E-mail: lengjs@hit.edu.cn

The ORCID identification number(s) for the author(s) of this article can be found under https://doi.org/10.1002/adfm.202408887

DOI: 10.1002/adfm.202408887

In recent years, with the rapid advancements in materials science and computational simulation technology, researchers have made remarkable progress in understanding and designing QZS metamaterials. A QZS metamaterial based on the origami concept has been proposed, which is capable of forming multiple ultra-wide longitudinal wave bandgaps at low frequencies, demonstrating great potential for suppressing longitudinal vibrations in engineering structures.[38] Furthermore, leveraging machine learning and optimization algorithms, researchers are exploring potential solutions for QZS metamaterials in a broader design space.[39] Inspired by typical bistable mechanical metamaterials, a novel design approach for programmable QZS metamaterials has been introduced.[40] Instead of parallel positive and negative stiffness units, optimized curved beams greatly simplify the design of QZS metamaterials. Although this design approach allows for proper modulation of QZS characteristics of metamaterials by assembling units, it presently showcases only the simplistic design of 2D units and their in-plane assembly, which limits its application in 3D spaces.

Building upon the design framework of simplistic QZS curved beams, this study presents a design methodology for compact QZS units and a novel three-level construction strategy to build 3D stair-stepping mechanical metamaterials (SMMs). These SMMs enable adjustable quantities and payloads of load plateaus from three distinct levels: unit, module, and 3D object, thereby generating stair-stepping force–displacement responses. Employing shape memory polymers (SMPs) known for their programmable and reconfigurable properties, SMMs with typical construction schemes were fabricated by 4D printing, enabling their satisfactory performance in vibration isolation through different methods. The first method capitalizes on the shape programmable attributes of the SMPs to apply an initial displacement corresponding to the load plateau. The second involves attaching additional mass equivalent to the plateau payload. The validity and accuracy of the design methods for the SMMs presented in this study have been tested and confirmed through experiments and finite element simulations.

2. Results and Discussion

2.1. Three-Level Construction Strategy for SMMs

A plateau appears in a typical force–displacement curve with QZS characteristics, which is defined by the plateau payload (F_0) and the plateau width (d_0) (**Figure 1a**). To facilitate the personalized customization of load plateau attributes in SMMs, a three-level (unit, module, and 3D object) construction strategy is proposed, as illustrated in Figure 1b. This approach embodies a reverse design concept that offers the potential to create 3D metamaterials matching the desired force–displacement response through multi-level assembly of units. Generally, the unit and the 3D object assembled from it do not exhibit the zero stiffness behavior in the unloaded state (state I). This zero stiffness characteristic fully emerges only when the unit is in a preloaded state, as depicted by the ideal zero stiffness curve in Figure 1c. In this preloaded state (state II), the unit has experienced an initial displacement u ($u_0 \le u < u_1$). If an additional displacement increment Δu ($0 < \Delta u \le u_1 - u$) is applied to the unit again, the load increment ΔF will be zero. When the unit in state II is assembled in multiple layers to form a 3D metamaterial, it will exhibit zero stiffness behavior during the initial loading phase, as depicted in Figure 1d. Figure S1 (Supporting Information) demonstrates the experimentally derived mechanical responses of the QZS unit under various states. Due to the influence of manufacturing and loading control accuracy, the force–displacement curve in state II does not fully exhibit zero stiffness characteristics, though it possesses a relatively low initial stiffness.

As described in the introduction section, SMMs can be utilized for low-band or even full-band vibration isolation due to their desirable QZS characteristics. When the unit is in state I, the SMM exhibits almost no vibration isolation capability for dynamic input disturbance. However, when the unit is transitioned to state II, dynamic input disturbance is effectively isolated across the entire frequency band (Figure 1e). To implement the free switching of QZS units between states I and II, two methods are proposed in this study. The first method leverages the shape memory effect of the SMP to program the shape of the unit, module, or 3D object. By employing a displacement u_0 (or $n \times u_0$ for a module with n units) to the unit in a high-temperature environment (above the SMP's glass transition temperature) and subsequently lowering the temperature, the programmed shape (state II) of the unit (or module) becomes fixed (Figure 1f). Notably, this programming process is reversible. The unit (or module) in state II can be actively reverted to state I by applying a thermal stimulus. Video S1 (Supporting Information) displays the programming process of the module utilizing the shape memory effect and the reversible shape recovery process. Consequently, this strategy outperforms conventional QZS isolators with only one or a limited number of load plateaus due to its ability to adjust the preload displacement according to the actual operating conditions. This allows for complete vibration isolation of the SMM from targets with varying weights (no greater than the plateau payload). For example, for an SMM with a QZS region characterized by a plateau payload of F_0 and an initial position of u_0, a preload displacement u_η (the displacement in the force–displacement curve corresponding to the load F_0-ηF_0) can be applied to the SMM when the weight of an object to be carried is ηF_0 ($0 < \eta \le 1$). The SMM will exhibit excellent vibration isolation performance when an object with a weight of ηF_0 is added in the programmed state (i.e., with the preload displacement u_η applied). The second method is to attach a mass block to the unit, module, or 3D object, with the weight of this mass block precisely matching the plateau payload on the force–displacement curve (Figure 1g).

2.2. Implementation Schemes of the Strategy

The foundation for achieving the aforementioned 3D SMMs with multiple pathways to zero stiffness lies in the construction of metamaterial units with desirable QZS characteristics. This is accomplished through the utilization of the non-uniform rational B-spline (NURBS) method, enabling the parametric optimal design of curved beams with a predefined load plateau.[40] In this design process, the shape of the curved beam in the design space is defined by a NURBS curve with six control points (P_1-P_6). P_1 [0, 0] and P_6 [l, h] are anchored at the corners of the design space, while P_2-P_5, i.e., [P_{ix}, P_{iy}] (i = 2, 3, 4, 5) serve as design variables (Figure S2a, Supporting Information). Horizontal motion at both

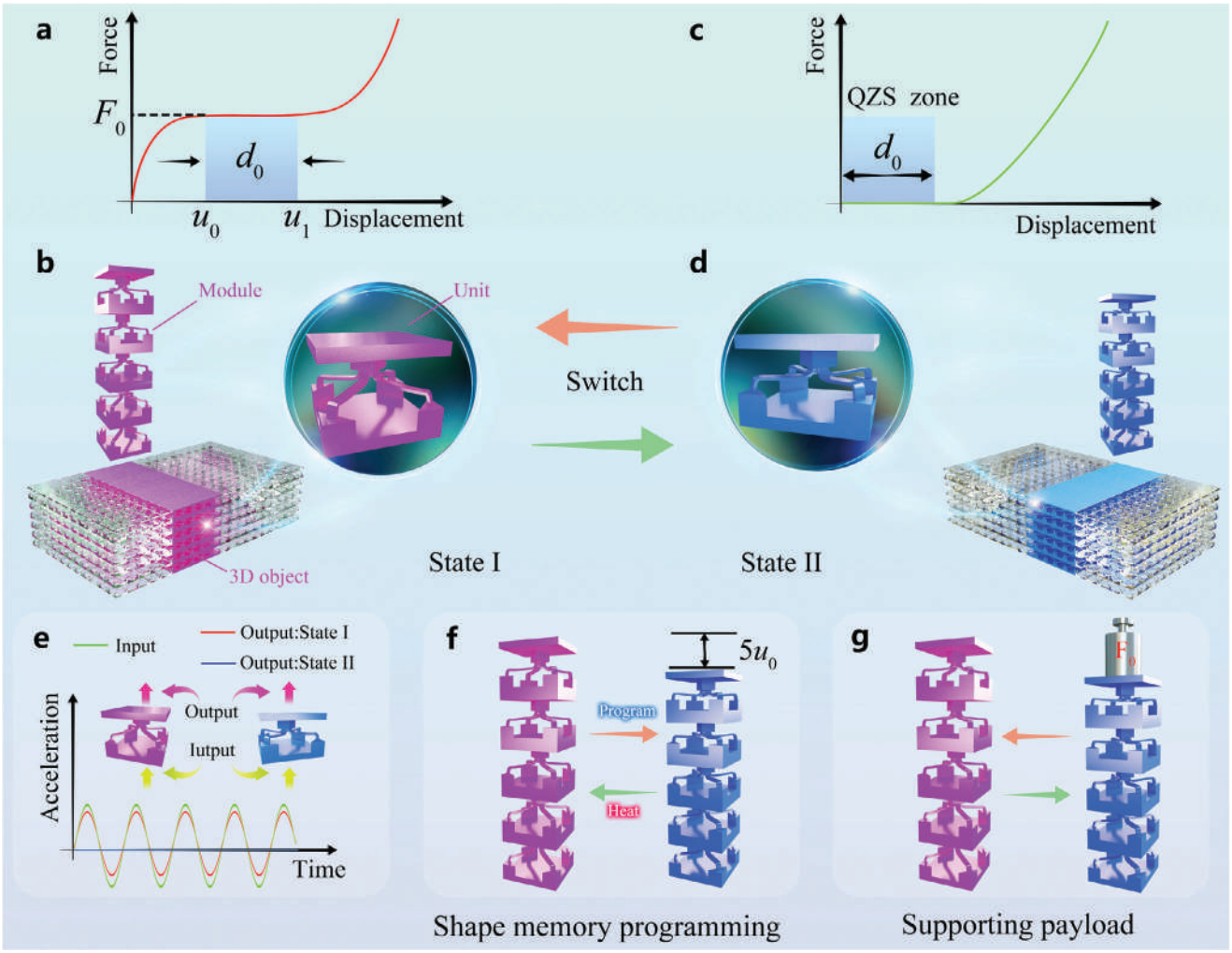

Figure 1. Schematic of the design of 3D SMMs with multiple pathways to zero stiffness. a,b) Force–displacement curve and three-level structure of the SMM in the initial state (state I). c,d) Force–displacement curve and three-level structure of the SMM in the programmed state (state II). e) Vibration isolation capability of SMMs in states I and II, where the SMM in state II is isolated from vibration nearly over the full frequency band. f,g) The programmed state of the SMM is obtained by applying the shape memory effect of SMP or attaching additional mass.

ends is constrained, and vertical displacement is applied to the end of the beam, where the reaction force is undertaken as a design object, with the aim of achieving the desired QZS characteristics. To ensure the load remains constant within the QZS zone, n target points are selected. Consequently, the design objective is to minimize the error between the actual force exerted by the curved beam and the ideal constant force at these n target points (Figure S2b, Supporting Information). By imposing appropriate constraints on the design variables, an implementation procedure is established for the geometrically optimized design of the curved beam. Further details on this process can be found in the Supporting Information.

Following the optimization procedure described earlier, the geometric parameters of the curved beam are determined as P_1 = [0 and 0 mm], P_2 = [0.345 and 3.698 mm], P_3 = [2.730 and 2.880 mm], P_4 = [9.375 and 4.028 mm], P_5 = [14.775 and 4.223 mm], and P_6 = [15 and 7.5 mm]. Subsequently, considering three different beam thicknesses (t = 0.7, 0.8, and 0.9 mm), the force–displacement curves for the curved beam with the above geometric parameters are generated through finite element simulations (Figure S2c, Supporting Information). The force–displacement curves corresponding to these three beam thicknesses exhibit the desired QZS characteristics. However, it is worth noting that the plateau payload increases significantly with increasing beam thickness. Throughout the loading process, the maximum principal strain within the curved beam remains below 0.035, signifying the feasibility of employing the linear elastic constitutive law to model the material behavior in finite element simulations (Figure S2d, Supporting Information). The finite element simulations are completed using the commercial finite element software ABAQUS/Standard. The curved beams are modeled by employing light-cured polylactic acid-based SMPs (PLA-based SMPs), with material properties characterized by ν = 0.4 and E = 0.68 GPa (Figure S3, Supporting Information).

Based on the optimized curved beams with QZS characteristics, a compact and symmetrical layout pattern is employed to construct QZS units. The four curved beams are arranged

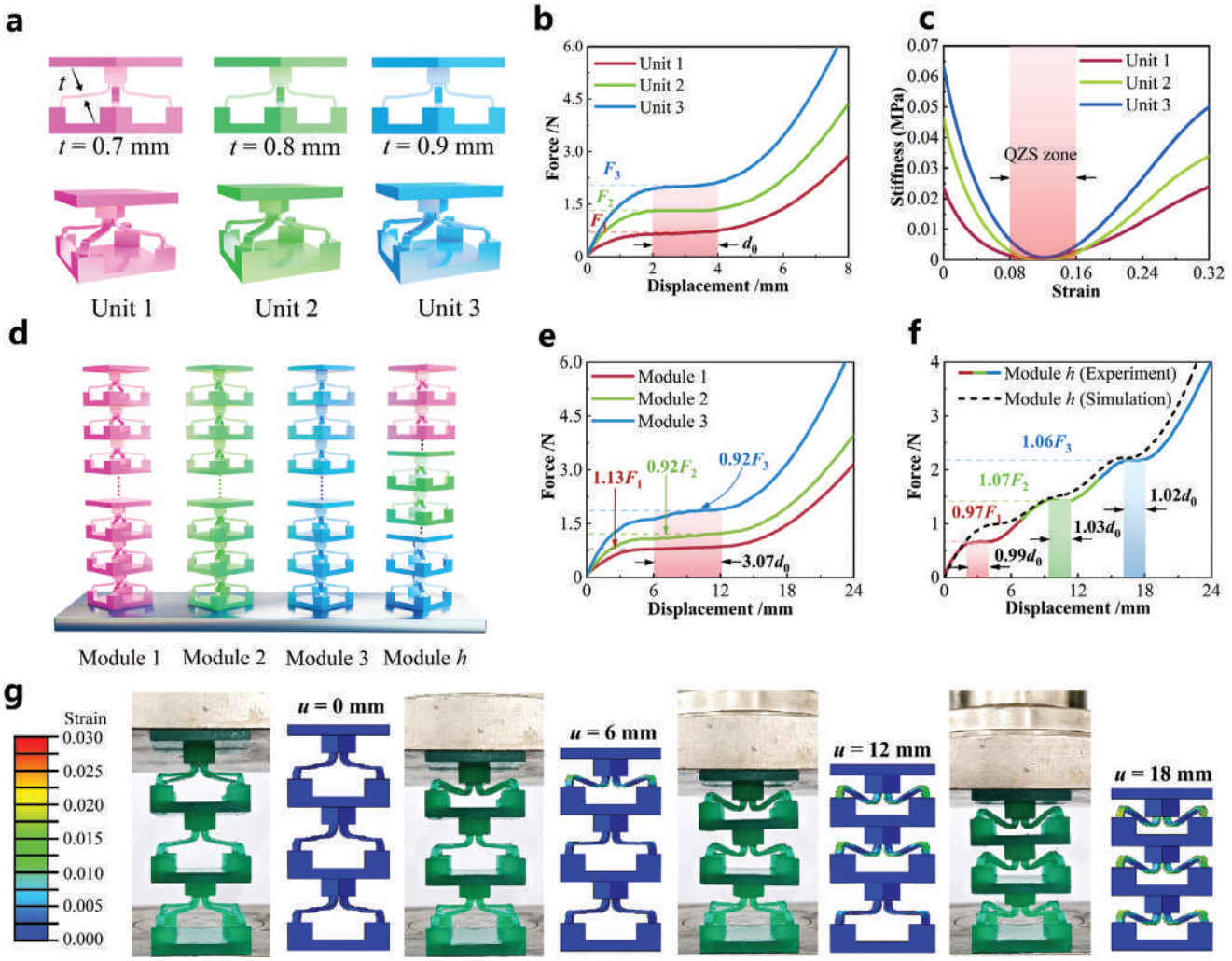

Figure 2. Mechanical behavior of QZS units and modules. a) Schematic diagram, b) force–displacement curves, and c) stiffness–strain curves of QZS units with various beam thicknesses *t*. d) Schematic diagram of QZS modules assembled from QZS units in series. e) Force–displacement curves of uniform modules with single load plateau. f) Force–displacement curves of the hybrid module with stair-stepping multiple load plateaus. g) Experiment and finite element simulation of the compressive deformation pattern for the hybrid module.

in a circular array, with thoughtfully designed piers to prevent any interference among the curved beams during the loading. Three types of units (Unit 1, Unit 2, and Unit 3) are constructed, all sharing the same geometric parameters except the beam thickness t (**Figure** 2a). The design details and specific dimensions of these three types of units are displayed in Figure S4 (Supporting Information). The experimental force–displacement curves of these three units demonstrate consistent plateau width d_0 (i.e., u_1-u_0) but distinct plateau payloads (Figure 2b). The plateau payloads for Unit 1, Unit 2, and Unit 3 are denoted as F_1, F_2, and F_3, respectively, in the order $F_1 < F_2 < F_3$. The stiffness–strain curves of these units are derived from the experimental force–displacement curve, revealing a trend where stiffness initially decreases from higher values to zero, followed by an increase to higher values again, thereby forming a distinct QZS zone (Figure 2c). Additionally, the force–displacement responses obtained from the finite element simulations are in excellent agreement with the measured responses, as presented in Figure S5 (Supporting Information). Meanwhile, the deformation configurations of units for loading displacements u = 0, 2, 4, and 6 mm (Figure S5, Supporting Information) indicate that the maximum principal strain of units during loading remains ≈3%.

In addition to the monotonic loading response described above, the multi-cycle loading and unloading behavior of the QZS units is evaluated in this study (Figure S6, Supporting Information). The cyclic response indicates that the loading and unloading curves cannot precisely coincide with each other, forming a phenomenon known as the "Mullins effect". This discrepancy is attributed to the inherent energy dissipation of the SMPs during the loading or unloading. Despite the energy dissipation, it is noteworthy that the unloading curve displays a load plateau similar to that observed in the loading curve. Besides, the hysteresis loop maintains nearly the same profile during the subsequent loading and unloading cycles, demonstrating the excellent reusability of the QZS units.

QZS modules are constructed by connecting multiple units in series (Figure 2d). Under static loading, each unit in the module shares the same loading force, but the displacement of the module is the cumulative sum of the displacements of all units. Consequently, by adjusting the number and type of units in the module, it becomes feasible to program the width and number of load plateaus, and even attain a stair-stepping configuration with multiple QZS workspaces. To illustrate this, three uniform modules (Module 1, Module 2, and Module 3) and one hybrid module (Module *h*) are constructed herein. Three uniform modules are composed of the same Unit 1, Unit 2, and Unit 3, while the hybrid module is assembled from different units. In all modules, the number of units is adjustable. When each module contains three units, the plateau width of the uniform modules approximates $3.07d_0$, which fundamentally represents the aggregate of the plateau widths (d_0) of three identical units (Figure 2e). The plateau payload of the uniform module is close to, but not precisely equal to, the plateau payload of the corresponding constituent unit. For instance, the measured value of the plateau payload for Module 1 is $\approx 1.13F_1$, deviating slightly from the ideal value F_1. This deviation primarily originates from errors in beam thickness introduced during 4D printing and external interferences during the test.

The experimental measurements and finite element simulations of the force–displacement curves for the uniform modules are presented in Figure S7 (Supporting Information), revealing a satisfactory agreement. Furthermore, the compression deformation process of the uniform modules is depicted in Figure S8 and Video S2 (Supporting Information). Finite element analysis shows nearly identical deformation patterns across the three units within each module. In contrast, experimental observations reveal slight disparities in deformation timing among the units in the same module, which is attributed to the subtle difference in the mechanical properties of the units due to the manufacturing precision. These disparities in deformation lead to imperfectly flat load plateaus in the force–displacement curves.

The experimental force–displacement curve for Module *h* exhibits a distinctive stair-stepping pattern, indicating the presence of multiple load plateaus (Figure 2f). Within the Module *h*, which comprises three different units (Unit 1, Unit 2, and Unit 3), the deformation during compression is not uniform. Specifically, Unit 1 enters the plateau phase first, followed by Unit 2, and finally Unit 3. Consequently, the three distinct plateau forces observed in the stair-stepping curve correspond to the plateau payloads of Unit 1, Unit 2, and Unit 3, respectively. Furthermore, an interesting observation is that the widths of these three plateaus in the stair-stepping curve are identical and approximately equal to the plateau width d_0 of the unit. As explicated in Figure 2g, the deformation pattern of Module *h* during compression follows a top-to-bottom segmental deformation, which is consistent with the analysis presented above. The finite element simulation also reveals a stair-stepping behavior in the force–displacement curve of Module *h*, with a less distinct load plateau corresponding to Unit 2. In the simulation, the four curved beams in Unit 2, uniform in material composition and geometric structure, are arranged in a circular pattern, thereby undergoing synchronous deformation. This synchronous deformation hampers the capacity of Unit 2 to balance the coupled effects from Unit 1 and Unit 3 during loading, potentially causing unevenness in the second plateau. In the experiment, limited manufacturing precision results in slight variations in the mechanical properties of the curved beams in Unit 2, inhibiting synchronous deformation. This variability enhances the capability of Unit 2 to modulate the impacts of Unit 1 and Unit 3, allowing the second load plateau in the experimental curve to maintain a more defined and flat characteristic.

To validate the universality of the aforementioned construction methods of QZS units and modules, the ranges of the key unit parameters *t*, *l*, and *h* are further extended. By setting the parameters *l* and *h* to 20 and 10 mm, respectively, the geometric configurations and compression responses of QZS units with varying beam thicknesses *t* are constructed, as illustrated in Figure S9 (Supporting Information). It is observed that when only the beam thickness varies, the width of the load plateau in the force–displacement curves of different units remains nearly equal, which is consistent with the experimental phenomena previously observed. Furthermore, uniform and hybrid modules are obtained by assembling three units in series. The uniform modules exhibit a widened single load plateau, while the hybrid module displays stair-stepping load plateaus, where the widths of each load plateau are nearly equal (Figures S10–S12, Supporting Information).

The adaptable load plateau achieved through the sequential connection of modules demonstrates the practical feasibility of the three-level construction strategy. This approach establishes a clear correspondence between the mechanical behavior and the structural characteristics of the metamaterial (**Figure 3a**). By using the target force–displacement relationship, structural details of the desired metamaterial can be rapidly determined through the modular unit assembly. To clarify the strategy and guide practical applications, the following three typical design schemes are proposed. It is important to note that the design approach for SMMs outlined in this study is both universal and inclusive, and is not confined to these three designated schemes.

Scheme 1: k_m identical modules (Module *m*) are arranged in parallel to form a 3D SMM, and Module *m* is assembled from q_m identical units (Unit *m*) in series (Figure 3b). This scheme is characterized by only one QZS zone in the force–displacement curve for the metamaterial with a width of $q_m d_0$ and a plateau payload of $k_m F_m$, where F_m refers to the plateau payload of Unit *m*.

Scheme 2: *m* different types of modules (Modules 1, 2,..., *m*) are assembled in parallel to form a 3D SMM. The quantity of Module *i* ($i = 1, 2, ..., m$) is k_i, each composed of q_i ($q_1 = q_2 = ... = q_m$) identical units (Unit *i*) assembled in series (Figure 3c). This scheme is defined by the fact that there is only one QZS zone with a width of $q_m d_0$ and a plateau payload $\sum_{i=1}^{m} k_i F_i$ on the force–displacement curve for the metamaterial, where F_i denotes the plateau payload of Unit *i*.

Scheme 3: k_m identical hybrid modules (Module *m*) are allocated in parallel to form a 3D SMM, and the hybrid module *m* is assembled by *m* different types of units (Units 1, 2,..., *m*) in series, where the number of Units *i* ($i = 1, 2, ..., m$) is q_i (Figure 3d). This scheme is characterized by the presence of *m* QZS zones in the force–displacement curve of the metamaterial, and the width and plateau payload of the *i*-th QZS zone are $q_i d_0$ and $k_i F_i$ ($k_1 = k_2 = ... = k_m$ and $F_1 < F_2 < ... < F_m$), respectively.

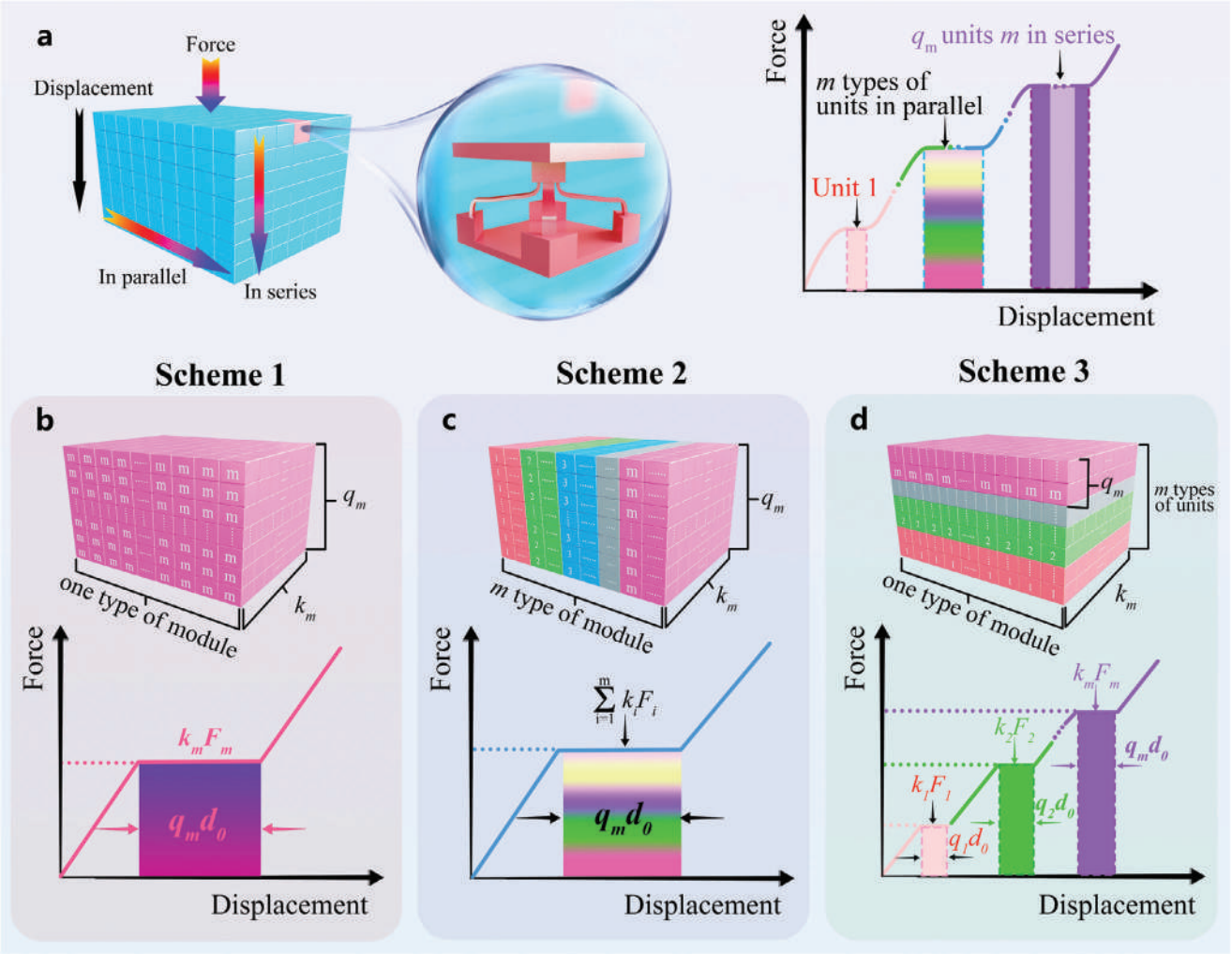

Figure 3. Implementation scheme of 3D SMMs with programmable load plateau. a) The graphical correspondence relation between plateau characteristics and structural details of metamaterials. b,c) SMM with single load plateau assembled in parallel from the same uniform modules (Scheme 1) and different uniform modules (Scheme 2). d) SMM with stair-stepping multiple load plateau assembled in parallel from the same hybrid modules (Scheme 3).

The above three schemes present various layouts of modules and units. A reasonably designed scheme can achieve arbitrary numbers and characteristics of QZS zones of the SMM. Scheme 1 involves the use of a single type of unit, resulting in a straightforward structural composition for the metamaterial, albeit with limited flexibility in payload design. In contrast, the metamaterial constructed based on Scheme 2 features an aggregate plateau payload ($\sum_{i=1}^{m} k_i F_i$) which can be finely tuned by adjusting both k_i and F_i ($i = 1, 2, \ldots, m$), giving substantial design flexibility. Scheme 3 provides an avenue to create 3D SMMs with the desired stair-stepping load plateaus. On the one hand, it is feasible to achieve a specific number of QZS zones by manipulating the number of unit types in the module. On the other hand, personalization of the width and plateau payload for the i-th QZS zone can be achieved by controlling the number of hybrid modules (Module m) and that of the i-th ($i = 1, 2, \ldots, m$) type of unit in Module m. It is worth mentioning that these three schemes are not exhaustive, and other schemes can also be employed to build 3D SMMs that match the target load plateaus. For instance, the SMMs with non-rectangular configurations, created by assembling modules with varying quantities of units, may showcase plateau characteristics that are both intricate and visually appealing.

2.3. Validation of Programmable Stair-Stepping Response

To verify the effectiveness of the three-level construction strategy in creating SMMs with programmable load plateaus, metamaterial prototypes are manufactured based on the above three schemes. All metamaterial prototypes consist of an array of six three-unit modules. In Scheme 1, Module 3, comprising three identical units (Unit 3), was chosen to construct the 3D SMM. Both experimental and finite element simulation results of the force–displacement curves for the metamaterial based on Scheme 1 reveal the expected single QZS zone (**Figure 4a**). The

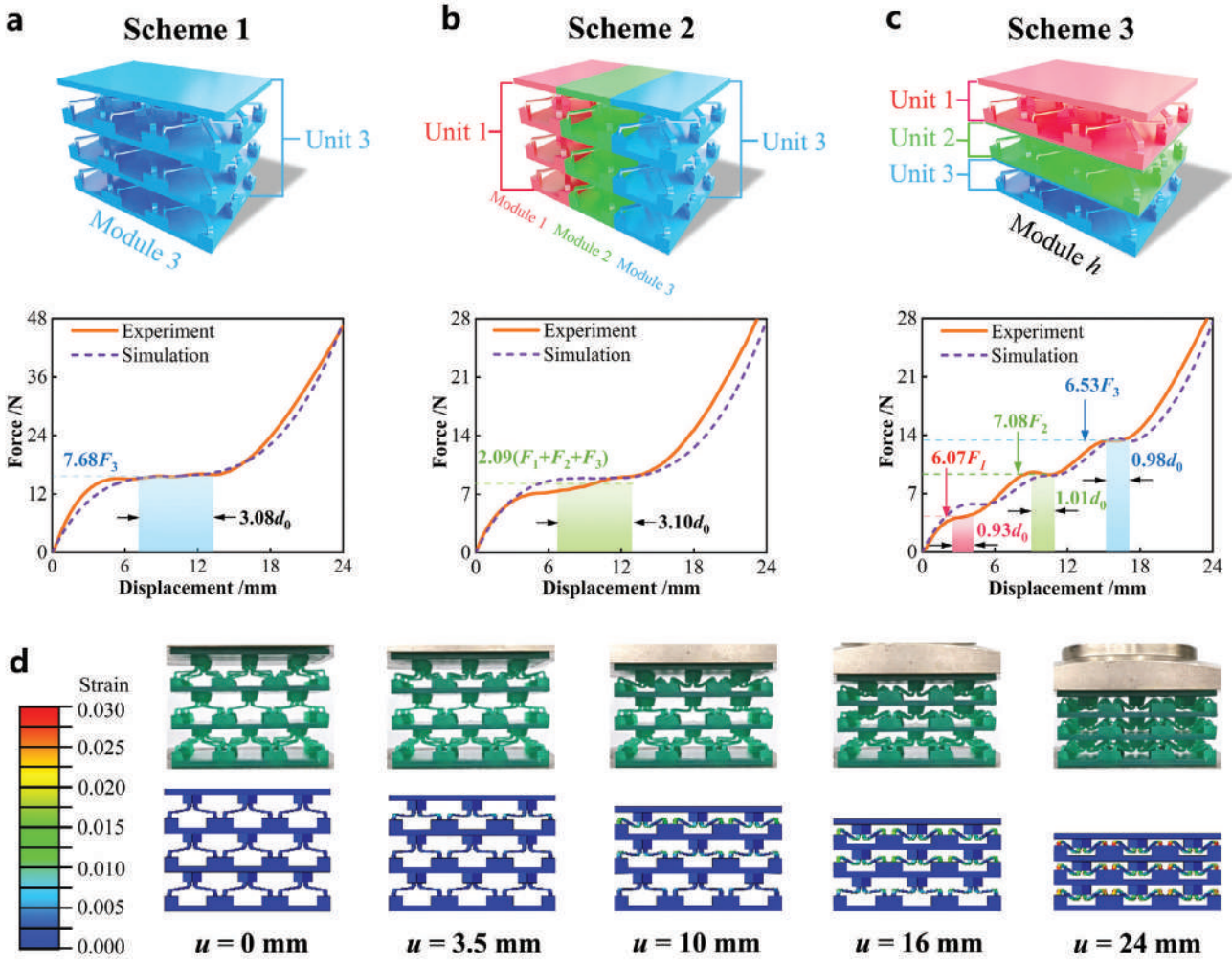

Figure 4. Mechanical behavior of 3D SMMs assembled by different schemes. Experimental and simulated validation of the force–displacement curves for the SMMs corresponding to a) Scheme 1, b) Scheme 2, and c) Scheme 3. d) Compressive deformation modes of the SMM corresponding to Scheme 3.

width of this zone is $3.08d_0$, which is nearly identical to that of the QZS zone in Module 3. The plateau payload in this zone is $7.68F_3$, exceeding the expected value of $6F_3$. This can be attributed to subtle differences in mechanical properties among identical units caused by the manufacturing process and loading conditions. As a result of these differences, the identical units connected in series do not enter the QZS zone at precisely the same rate, leading to load fluctuations.[41] Moreover, the SMM corresponding to Scheme 1 is constructed from multiple identical modules connected in parallel, where the geometric constraints between modules are not eliminated, thus the coupling effect between the modules further complicates the evolution of the plateau payload.

In Scheme 2, three types of uniform modules (Module 1, Module 2, and Module 3) are employed, as demonstrated in Figure 4b. The experimental force–displacement curve undergoes some load fluctuations in the QZS zone, whereas the simulated curve demonstrates a consistent plateau payload. The theoretical payload corresponding to this scheme is $2(F_1+F_2+F_3)$, while the experimental value is $2.11(F_1+F_2+F_3)$, indicating excellent agreement between experimental and theoretical values. In Scheme 3, a gradient SMM whose force–displacement profile exhibits stair-stepping multiple QZS zones (Figure 4c) is established by employing the hybrid module (Module h). Three QZS zones, each with approximately the same width (approximately d_0), are observed, and the plateau payload presents a stepwise increasing trend. More complex stair-stepping force–displacement curves can be achieved by further adjusting the number of hybrid modules in parallel or the type of units in the hybrid module (Figure S13, Supporting Information). Typical deformation states of the SMM obtained by Scheme 3 during loading are depicted in Figure 4d. It is evident from above analysis that the deformation states at u = 3.5, 10, and 16 mm in Figure 4d correspond to the three plateaus in Figure 4c, respectively. During each plateau phase, no deformation is observed in the layers except for the layer corresponding to the specific plateau, as they do not "sense" the changes in resultant force.

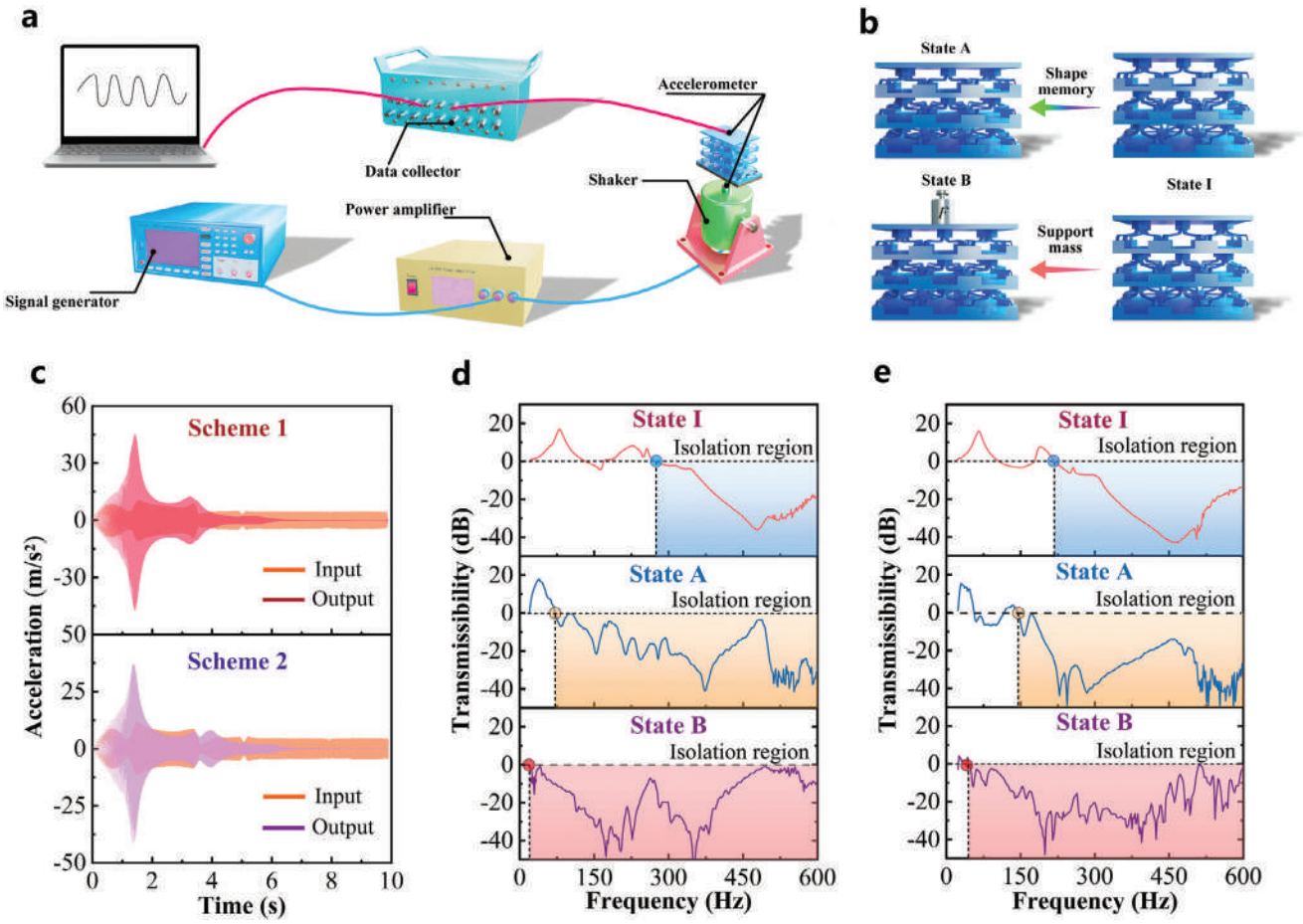

Figure 5. Vibration isolation properties of SMMs with one load plateau. a) Vibration testing system. b) Initial state (state I) and programming states (state A and state B) of the SMM. c) The input and output acceleration amplitudes for SMMs in state I over time. d,e) The experimental transmittance curves of SMMs corresponding to Scheme 1 and Scheme 2 in different states.

The above analysis and discussion have demonstrated the feasibility of tailoring SMMs with programmable load plateau through the three-level construction strategy. Subsequently, the vibration isolation effect of these SMMs is verified via a series of vibration tests. As given in **Figure** 5a, the vibration testing system comprises a signal generator, a power amplifier, a modal shaker, two accelerometers, a data collector, and a computer. The SMM prototype is securely mounted onto the modal shaker, with two accelerometers affixed to its lower and upper surfaces, respectively. The sinusoidal acceleration signal generated by the signal generator is amplified employing a power amplifier and subsequently applied to the SMM by the shaker. This signal is detected by the accelerometer on the lower surface, while the resultant acceleration response is continuously monitored by the accelerometer on the upper surface. According to the two methods for achieving low-frequency vibration isolation, three distinct states of the SMM, namely state I, state A, and state B, are defined. These three states correspond to the unloaded state, the shape memory programming state, and the supporting payload state, respectively, as depicted in Figure 5b.

Furthermore, the vibration isolation performances of SMMs corresponding to the three schemes in Figure 4 are evaluated. In the case of both Schemes 1 and 2, the metamaterial features a single load plateau, consequently allowing for only one shape memory programming state (state A) and one supporting payload state (state B), both of which facilitate full-band vibration shielding capability. In the unloaded state (State I), the acceleration amplitude over time for the SMMs utilizing Schemes 1 and 2 under sinusoidal sweep excitation is depicted in Figure 5c. At the initial stage of vibration excitation, the output acceleration significantly exceeds the input acceleration, indicating amplification of vibration in the low-frequency band.

To access the low-frequency vibration isolation capability of the SMM in states A and B, the transmittance is defined as $20\log_{10}(A_{out}/A_{in})$, where A_{in} represents the input acceleration amplitude and A_{out} signifies the output acceleration amplitude.[42] For Scheme 1, the implementation of the shape memory programming (from state I to state A) leads to a noteworthy reduction in both the resonant frequency and the vibration isolation frequency (the onset frequency of the vibration isolation region) of the SMM. Specifically, the vibration isolation frequency decreases from 273.4 to 70.4 Hz, thereby achieving effective vibration damping in the lower frequency band (Figure 5d). When the SMM associated with Scheme 1 transitioned from state I to state

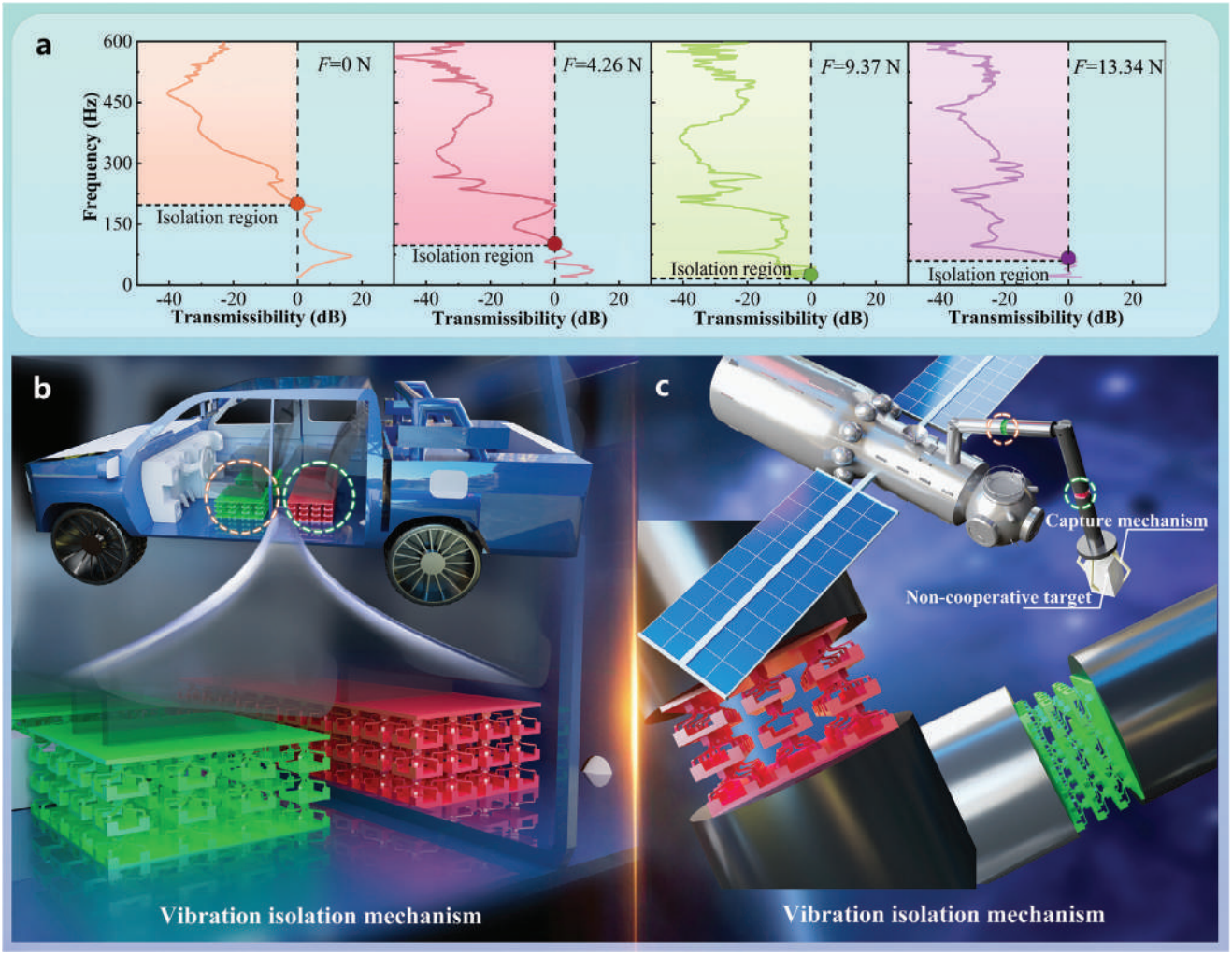

Figure 6. Vibration isolation properties and applications of SMMs with multiple load plateaus. a) Transmittance curves of the SMM under Scheme 3 at varying supporting loads, with three of which corresponding to plateau payloads. b) The SMM as a vibration isolation mechanism for vibration damping in automotive seats. c) The SMM mounted between the satellite platform and the capture mechanism for vibration suppression.

B by supporting payload (equivalent to the plateau payload), the vibration isolation frequency experienced a further reduction to 18.9 Hz, thus reaching ultra-low frequency vibration isolation. Similarly, for Scheme 2, the vibration isolation performances of the SMM under two methods are improved (Figure 5e).

The SMM in Scheme 3 boasts stair-stepping multiple load plateaus, allowing for vibration shielding under diverse operational conditions by applying the corresponding plateau payloads. As explicated in Figure 4c, three plateau payloads, measuring 4.26, 9.37, and 13.34 N, respectively, are evident. The transmittance curves corresponding to these plateau payloads are plotted in **Figure** 6a. Comparing these conditions to the unloaded state ($F = 0$ N), supporting payload yields a substantial improvement in vibration isolation performance. Especially, in the second payload state (F = 9.37 N), the vibration isolation frequency decreases from 201.9 to 17.6 Hz, demonstrating nearly full-band vibration isolation. However, the vibration isolation frequencies for the first and third payload cases are 99.1 and 60.9 Hz, respectively. The limited low-frequency isolation capability can be attributed to the non-standard load plateaus in the QZS region of the force–displacement curve (Figure 4c).

The proposed SMMs with programmable load plateaus possess versatile applications, including vibration isolation mechanisms in the automotive industry to achieve effective vibration damping of safety seats. As illustrated in Figure 6b, SMMs featuring stair-stepping payloads and closely spaced load intervals, constructed utilizing the three-level construction strategy, are integrated between the vehicle seat and the platform. This setup effectively shields occupants from vibration-induced damage across a broad range of loads. Another noteworthy application of SMMs is their utilization as vibration isolation mechanisms positioned between the on-orbit capture mechanism or manipulator and the satellite platform. This application aims to mitigate the vibration excitations resulting from capture operations, thereby eliminating the adverse impact of vibrations on other vibration-sensitive instruments (Figure 6c). The vibration isolation mechanism effectively dampens the periodic excitation or shocks generated by the capture mechanism during the

non-cooperative target capture process, ensuring that minimal vibration is transmitted to the satellite platform.

3. Conclusion

In this study, an innovative three-level construction strategy is proposed to build 4D printed SMMs with programmable load plateaus from three levels: unit, module, and 3D object. Three typical design schemes are also proposed to demonstrate the effectiveness of the strategy in customizing the number of load plateaus and QZS characteristics within the force–displacement profile. This study has resulted in the creation of single QZS-zone metamaterials with programmable plateau width and payload as well as multiple QZS-zone metamaterials with stair-stepping plateaus. These designs have been rigorously validated through experiments and finite element simulations. In addition, these metamaterials possess versatility in vibration isolation, allowing efficient switching between high-frequency and medium or low-frequency bands by altering the unit configuration between the initial and programmed states. This configurational switching is reversible and can be achieved through two methods: shape memory programming and supporting payload. In conclusion, the innovative concept of SMMs offers a clear path for customizing force–displacement profiles using reverse engineering principles, opening the door to achieving multimodal vibration isolation for cutting-edge precision devices.

4. Experimental Section

Fabrication of SMMs: Three types of units (Unit 1, Unit 2, and Unit 3), four types of modules (Module 1, Module 2, Module 3, and Module *h*), and three distinct 3D SMMs (Scheme 1, Scheme 2, and Scheme 3) were fabricated by using light-curing 4D printing. For the printing material, a PLA-based photocurable liquid polymer (eSUN-PLA) purchased from eSUN was employed as the photocurable SMP precursor solution. The printing process was carried out employing a laser cladding deposition 3D printer (Anycubic Photon M3 Plus). This printer features an UV light wavelength of 405 nm, XY-axis pixel resolution of 0.034 mm, and Z-axis pixel resolution of 0.01 mm.

Mechanical Testing: The quasi-static mechanical testing was conducted on the SMMs in compression mode using an electronic universal testing machine (ZwickRoell Z010). The test involves positioning the sample between two clamps on the testing machine, with displacement applied at a rate of 4 mm min^{-1}. The loading direction was aligned parallel to the stacking direction of the units in the module. Details of the mechanical testing equipment and samples are presented in Figure S14a,b (Supporting Information).

Vibration Testing: The vibration testing system consists of several key components, including a signal generator (KEYSIGHT 33500B), a power amplifier (LA-200), a modal shaker (YMC MS-100), two accelerometers (PCB 352), and a data collector (DH5956). The SMM prototype was securely attached in a vertical orientation to the shaker employing a custom fixture. This setup was designed to eliminate any influence from bending-induced vibrations of the mandrel on out-of-plane vibration. The vibration excitation, generated as a sinusoidal sweeping waveform, was produced by the signal generator. This signal was then amplified by the power amplifier and subsequently applied to the SMM through the modal shaker. The input and output acceleration signals in the time domain were captured by accelerometers and data collectors and converted to frequency response curves. The modal shaker and the SMM prototype used for vibration testing are shown in Figure S14c,d (Supporting Information).

Finite Element Simulations: Quasi-static simulations were performed on the compression behavior of 4D printed SMMs using the commercial finite element software ABAQUS/Standard. The models were created by the computer-aided design in SOLIDWORKS 2016 and are meshed with an eight-node brick element (C3D8R). The mesh convergence analysis was carried out (Figure S15, Supporting Information), and the element size is ultimately set to 0.4 mm to balance simulation accuracy and computational efficiency. Additionally, geometric nonlinearity was considered to accommodate the large bending deformation experienced by the curved beams during loading. Furthermore, the PLA-based SMP was represented using an elastic constitutive law with a Young's modulus of 0.68 GPa and a Poisson's ratio of 0.4 (Figure S3, Supporting Information).

Supporting Information

Supporting Information is available from the Wiley Online Library or from the author.

Acknowledgements

This work was financially supported by the National Key R&D Program of China (Grant No. 2022YFB3805700), the National Natural Science Foundation of China (Grant No. 12072094), the China Postdoctoral Science Foundation (Grant No. 2023M730870), and the Postdoctoral Fellowship Program of CPSF (Grant No. GZB20230957).

Conflict of Interest

The authors declare no conflict of interest

Data Availability Statement

The data that support the findings of this study are available from the corresponding author upon reasonable request.

Keywords

4D printing, load plateaus, shape memory polymers, stair-stepping mechanical metamaterials, vibration isolation

Received: May 23, 2024
Revised: June 23, 2024
Published online:

[1] D. Wang, L. Dong, G. Gu, *Adv. Funct. Mater.* **2022**, *33*, 2208849.
[2] K. Bertoldi, V. Vitelli, J. Christensen, M. van Hecke, *Nat. Rev. Mater.* **2017**, *2*, 17066.
[3] A. J. D. Shaikeea, H. Cui, M. O'Masta, X. R. Zheng, V. S. Deshpande, *Nat. Mater.* **2022**, *21*, 297.
[4] Y. Liu, F. Pan, F. Xiong, Y. Wei, Y. Ruan, B. Ding, K. Yang, Y. Chen, *Adv. Funct. Mater.* **2023**, *33*, 2300433.
[5] Y. Wu, Y. Han, Z. Wei, Y. Xie, J. Yin, J. Qian, *Adv. Funct. Mater.* **2023**, *33*, 2306442.
[6] W. Zhao, J. Zhu, L. Liu, J. Leng, Y. Liu, *Int. J. Smart Nano Mater.* **2022**, *14*, 1,
[7] J.-H. Bastek, D. M. Kochmann, *Nat. Mach. Intell.* **2023**, *5*, 1466.
[8] D. M. J. Dykstra, C. Lenting, A. Masurier, C. Coulais, *Adv. Mater.* **2023**, *35*, 2301747.

[9] J. Qi, Z. Chen, P. Jiang, W. Hu, Y. Wang, Z. Zhao, X. Cao, S. Zhang, R. Tao, Y. Li, D. Fang, *Adv. Sci.* **2022**, *9*, e2102662.
[10] H. Ye, Q. Liu, J. Cheng, H. Li, B. Jian, R. Wang, Z. Sun, Y. Lu, Q. Ge, *Nat. Commun.* **2023**, *14*, 1607.
[11] F. Pan, Y. Li, Z. Li, J. Yang, B. Liu, Y. Chen, *Adv. Mater.* **2019**, *31*, 1900548.
[12] Q. Zhang, J. Dong, Y. Zhao, Y. Zheng, *Int. J. Smart Nano Mater.* **2022**, *13*, 152.
[13] L. Du, W. Shi, H. Gao, H. Jia, Q. Zhang, M. Liu, Y. Xu, *Adv. Funct. Mater.* **2024**, 2314123.
[14] P. Jiao, J. Mueller, J. R. Raney, X. Zheng, A. H. Alavi, *Nat. Commun.* **2023**, *14*, 6004.
[15] P. Jiao, *Prog. Mater. Sci.* **2023**, *137*, 101132.
[16] C. Yue, W. Zhao, F. Li, B. Li, L. Liu, Y. Liu, J. Leng, *Adv. Funct. Mater.* **2024**, 2316181.
[17] T. Mei, Z. Meng, K. Zhao, C. Q. Chen, *Nat. Commun.* **2021**, *12*, 7234.
[18] X. Fang, J. Wen, L. Cheng, D. Yu, H. Zhang, P. Gumbsch, *Nat. Mater.* **2022**, *21*, 869.
[19] A. Farzaneh, N. Pawar, C. M. Portela, J. B. Hopkins, *Nat. Commun.* **2022**, *13*, 1041.
[20] X. Guo, X. Ni, J. Li, H. Zhang, F. Zhang, H. Yu, J. Wu, Y. Bai, H. Lei, Y. Huang, J. A. Rogers, Y. Zhang, *Adv. Mater.* **2020**, *33*, 2004919,
[21] G. Librandi, E. Tubaldi, K. Bertoldi, *Nat. Commun.* **2021**, *12*, 3454.
[22] C. Coulais, E. Teomy, K. de Reus, Y. Shokef, M. van Hecke, *Nature* **2016**, *535*, 529.
[23] W. Liu, H. Jiang, Y. Chen, *Adv. Funct. Mater.* **2022**, *32*, 2109865.
[24] Q. Zhang, Y. Sun, *Int. J. Mech. Sci.* **2024**, *268*, 109024.
[25] X. Xu, Q. Wu, Y. Pang, Y. Cao, Y. Fang, G. Huang, C. Cao, *Adv. Funct. Mater.* **2021**, *32*, 2107896.
[26] J. Choi, T. Hong, D.-E. Lee, T. Cho, H. S. Park, *Int. J. Mech. Sci.* **2024**, *267*, 109004.
[27] Z. Wang, Q. Zhang, K. Zhang, G. Hu, *Adv. Mater.* **2016**, *28*, 9857.
[28] J. Park, G. Lee, H. Kwon, M. Kim, J. Rho, *Adv. Funct. Mater.* **2024**, 2403550.
[29] Z. Hu, Z. Wei, K. Wang, Y. Chen, R. Zhu, G. Huang, G. Hu, *Nat. Commun.* **2023**, *14*, 1266.
[30] L. Sangiuliano, B. Reff, J. Palandri, F. Wolf-Monheim, B. Pluymers, E. Deckers, W. Desmet, C. Claeys, *Mech. Syst. Signal Pr.* **2022**, *179*, 109335.
[31] Z. Wu, H. Li, X. Kong, Z. Deng, *Mech. Syst. Signal Pr.* **2023**, *186*, 109818.
[32] K. K. Dudek, J. A. Iglesias Martínez, G. Ulliac, L. Hirsinger, L. Wang, V. Laude, M. Kadic, *Adv. Mater.* **2023**, *35*, 2210993.
[33] J. Liu, Y. Wang, S. Yang, T. Sun, M. Yang, W. Niu, *Int. J. Mech. Sci.* **2024**, *269*, 108958.
[34] G. Yan, H.-X. Zou, S. Wang, L.-C. Zhao, Z.-Y. Wu, W.-M. Zhang, *Mech. Syst. Signal Pr.* **2022**, *162*, 108010.
[35] G. Gatti, A. D. Shaw, P. J. P. Gonçalves, M. J. Brennan, *Mech. Syst. Signal Pr.* **2022**, *164*, 108258.
[36] Y. Chai, X. Jing, X. Chao, *Int. J. Mech. Sci.* **2022**, *218*, 107077.
[37] X. Chong, Z. Wu, F. Li, *Mech. Syst. Signal Pr.* **2022**, *179*, 109352.
[38] H. Wan, H. Chen, Y. Wang, X. Fang, Y. Liu, K. Kosiba, *Virtual. Phys. Prototyp.* **2024**, *19*, 2299691.
[39] H. Kim, S. H. Tawfick, W. P. King, *Adv. Intell. Syst.* **2022**, *4*, 2200225.
[40] Q. Zhang, D. Guo, G. Hu, *Adv. Funct. Mater.* **2021**, *31*, 2101428.
[41] X. Lin, F. Pan, K. Yang, J. Guan, B. Ding, Y. Liu, K. Yang, B. Liu, Y. Chen, *Adv. Funct. Mater.* **2021**, *31*, 2101808.
[42] Y. Jin, S. Zeng, Z. Wen, L. He, Y. Li, Y. Li, *Mater. Des.* **2022**, *215*, 110499.